catalysts

MDPI

Article

Enhanced Photocatalytic and Photoluminescence Properties Resulting from Type-I Band Alignment in the Zn_2GeO_4/g-C_3N_4 Nanocomposites

Victor Y. Suzuki [1], Luis H. C. Amorin [1,2], Guilherme S. L. Fabris [3,4], Swayandipta Dey [5,6], Julio R. Sambrano [4], Hagai Cohen [7], Dan Oron [6] and Felipe A. La Porta [1,8,*]

1 Nanotechnology and Computational Chemistry Laboratory, Federal University of Technology—Paraná, Londrina 86036-370, PR, Brazil; victoryuudisuzuki@gmail.com (V.Y.S.); luis.amorin@gmail.com (L.H.C.A.)
2 Institute of Science, Technology and Innovation, Federal University of Bahia, Camaçari 42809-000, BA, Brazil
3 Department of Materials Engineering, Federal University of Rio Grande do Norte, Natal 59078-970, RN, Brazil; guilhermeslfabris@gmail.com
4 Modeling and Molecular Simulation Group, São Paulo State University, Bauru 17033-360, SP, Brazil; sambrano@fc.unesp.br
5 Department of Applied Physics and Institute for Complex Molecular Systems (ICMS), Eindhoven University of Technology, Postbus 513, 5600 MB Eindhoven, The Netherlands; s.dey@tue.nl
6 Department of Physics of Complex Systems, Weizmann Institute of Science, Rehovot 7610001, Israel; dan.oron@weizmann.ac.il
7 Department of Chemical Research Support, Weizmann Institute of Science, Rehovot 7610001, Israel; hagai.cohen@weizmann.ac.il
8 Post-Graduation Program in Chemistry, State University of Londrina, Londrina 86057-970, PR, Brazil
* Correspondence: felipelaporta@utfpr.edu.br

check for updates

Citation: Suzuki, V.Y.; Amorin, L.H.C.; Fabris, G.S.L.; Dey, S.; Sambrano, J.R.; Cohen, H.; Oron, D.; La Porta, F.A. Enhanced Photocatalytic and Photoluminescence Properties Resulting from Type-I Band Alignment in the Zn_2GeO_4/g-C_3N_4 Nanocomposites. *Catalysts* **2022**, *12*, 692. https://doi.org/10.3390/catal12070692

Academic Editors: Biljana F. Abramovic and Tamara B. Ivetić

Received: 10 May 2022
Accepted: 22 June 2022
Published: 24 June 2022

Publisher's Note: MDPI stays neutral with regard to jurisdictional claims in published maps and institutional affiliations.

Abstract: Well-defined Zn_2GeO_4/g-C_3N_4 nanocomposites with a band alignment of type-I were prepared by the ultrasound-assisted solvent method, starting from g-C_3N_4 nanosheets and incorporating 0, 10, 20, and 40 wt% of Zn_2GeO_4. In this study, we have investigated in-depth the photoluminescence emission and photocatalytic activity of these nanocomposites. Our experimental results showed that an increased mass ratio of Zn_2GeO_4 to g-C_3N_4 can significantly improve their photoluminescence and photocatalytic responses. Additionally, we have noted that the broadband photoluminescence (PL) emission for these nanocomposites reveals three electronic transitions; the first two well-defined transitions (at ca. 450 nm and 488 nm) can be attributed to $\pi^* \rightarrow$ lone pair (LP) and $\pi^* \rightarrow \pi$ transitions of g-C_3N_4, while the single shoulder at ca. 532 nm is due to the oxygen vacancy (Vo) as well as the hybridization of 4s and 4p orbital states in the Zn and Ge belonging to Zn_2GeO_4. These experimental findings are also supported by theoretical calculations performed under periodic conditions based on the density functional theory (DFT) fragment. The theoretical findings for these nanocomposites suggest a possible strain-induced increase in the Zn-O bond length, as well as a shortening of the Ge-O bond of both tetrahedral [ZnO_4] and [GeO_4] clusters, respectively. Thus, this disordered structure promotes local polarization and a charge gradient in the Zn_2GeO_4/g-C_3N_4 interface that enable an efficient separation and transfer of the photoexcited charges. Finally, theoretical results show a good correlation with our experimental data.

Keywords: g-C_3N_4/Zn_2GeO_4; optical and photocatalytic properties; band alignment; nanocomposites; DFT calculations

1. Introduction

Of course, the persistent population growth aligned with the fast industrial expansion also brought serious environmental problems; currently, the water pollution by synthetic organic dyes is one of the biggest reasons for concern [1–4]. As is well-known, about 7×10^5 tons of synthetic organic dyes are annually used by the textile industry [4,5]. Even

at low concentrations, such dyes are highly mutagenic, carcinogenic, and in addition less-biodegradable [6]. Consequently, in this perspective, the treatment of complex organic pollutants has been prioritized and well regulated by diverse countries. Thus, various strategies have been employed to the treatment of effluent with complex features (e.g., adsorption, biological degradation, membrane separation, photocatalysis, and so on), with more and more researchers paying attention to the development as well as application of heterostructured semiconducting materials-based photocatalysts [5–11]. Particularly, the photocatalysis has been considered as the most-efficient low-cost strategy to the treatment of effluent, resulting in a fast and non-selective oxidation of diverse pollutants [6,12]. Furthermore, the use of heterostructured semiconducting materials (or composites) in such applications can, in principle, lead to improving the efficient separation of the photoexcited charges, resulting in more efficient treatment of complex organic pollutants [11].

Among the different semiconducting materials proposed for this purpose, in particular the combination between the graphitic carbon nitride (g-C_3N_4) and zinc germanate (Zn_2GeO_4) in the form of nanocrystals, owing to its excellent properties, has aroused a great deal of recent interest in this field [13–15]. In additional, it is well-known that both materials are widely used in the photocatalytic decomposition of water into H_2 and O_2, and in organic photosynthesis, pollutant degradation, and other applications [13–20]. In practice, the electronic structure resulting from this combination between the g-C_3N_4 and Zn_2GeO_4 is dependent on the strategy of synthesis used, because it is extremely sensitive to changes in size, morphology, structure, composition, as well as imperfections in these parameters, which dictate their functional properties and desired technological applications [21–23].

Ongoing studies have focused on a fundamental understanding of the electronic structure of nanocomposites [24–26]. In such cases, it is widely known that computational materials design methods are robust tools for this type of study and, hence, have a pivotal role in elucidating the electronic structure of several advanced materials, i.e., contributing to accelerating the development of better materials [21–26]. Moreover, it is important to note that certain materials' properties are difficult to be experimentally measured. Many of these limitations, however, may be circumvented from a theoretical point of view. Among the computational tools for the theoretical understanding of solid materials' properties, in particular, the density functional theory (DFT) method under periodic conditions is one of the most used for obtaining a highly accurate prediction of their bandgap energy, the density of states, Fermi energy level, dielectric constants, effective mass, binding energy, structural, vibrational, and thermodynamic parameters, and others [21–31]. In this way, we highlight that these computational methodologies have played a growing role in developing sustainable next-generation advanced materials and is typically at the forefront of modern scientific research. However, due to the novelty of the Zn_2GeO_4/g-C_3N_4 nanocomposites, to the best of our knowledge, theoretical works on this system remain scarce in the literature. For this reason, a better and deeper understanding of the main interface features of these nanocomposites designed is an exciting topic of research for studying a large variety of physical nanoscale phenomena.

Here, we prepared well-defined Zn_2GeO_4/g-C_3N_4 nanocomposites (with 10, 20, and 40 wt% Zn_2GeO_4), with a type-I band alignment, using an ultrasound-assisted solvent method, and further investigated the effect of structural defects on their optical and photocatalytic properties. Methylene blue (MB) in solution was selected as a typical contaminant to evaluate the photocatalytic performance of these nanocomposites. Moreover, we used theoretical calculations, based on the periodic DFT method using the HSE06 functional, which includes dispersion effects, with an all-electron basis set for a reliable description of their electronic structure.

2. Results and Discussion

Figure 1a illustrates the powder X-ray diffraction (PXRD) patterns of the Zn_2GeO_4/g-C_3N_4 nanocomposites with 10, 20, and 40 wt% Zn_2GeO_4. In the PXRD patterns, all diffraction peaks could be perfectly indexed to the hexagonal structure of g-C_3N_4 (belonging

to space group P6m2) and the rhombohedral structure of Zn_2GeO_4 (belonging to space group R3) according to the Joint Committee on Powder Diffraction Standards (JCPDS) card numbers 87–526 and 11–687, respectively. With increasing content of Zn_2GeO_4, the measured angles for the (002) diffraction peak of the g-C_3N_4 structure were in the sequence of 2θ = 27.37°, 27.33°, 27.28°, and 27.43°, respectively. This variation reflects an alteration in the interplanar distance between neighboring sheets of g-C_3N_4, in accordance with previous studies [32–34]. Additionally, we also characterized the surface composition and structure of the Zn_2GeO_4/g-C_3N_4 nanocomposites by X-ray photoelectron spectroscopy (XPS). The XPS survey spectra in Figure 1b, comparing the 40 wt% Zn_2GeO_4/g-C_3N_4 nanocomposite with the two pure references, Zn_2GeO_4 and g-C_3N_4, demonstrate the overall purity of the composite. A more detailed XPS-based compositional analysis (see also the experimental section) further presents good agreement with the expected atomic concentrations and elemental oxidation states, reported in the literature [35–37]. As shown in Figure 1c, the bands observed in Fourier transform infrared spectroscopy (FTIR) measurements for the range 1236 cm^{-1} to 1555 cm^{-1} are usually attributed to C–N bonds of the heterocycles, and the 1640 cm^{-1} band is characteristic of the stretching of C=N bonds in g-C_3N_4. The sharp peak at 807 cm^{-1} is characteristic of the tri-s-triazine ring [31,38–40]. Other bands observed in the range of 3000 cm^{-1} to 3500 cm^{-1} correspond to the O-H and N-H stretching of adsorbed water molecules and free amino groups, respectively [31,38–40]. Moreover, small peaks that show up only in the composites, at approximately 530 cm^{-1} and 750 cm^{-1}, are attributed to the O-Zn-O and O-Ge-O stretching vibrations, respectively, of Zn_2GeO_4 [41–43].

Photoluminescence (PL) emission spectra obtained at room temperature are shown in Figure 1d. In this case, the broad PL emission profile for these nanocomposites reveals three electronic transitions, in good agreement with the structure previously elucidated by PXRD and FTIR. As expected, the first two well-defined transitions (at ca. 450 nm and 488 nm) can be attributed to $\pi^* \rightarrow$ LP and $\pi^* \rightarrow \pi$ transitions of g-C_3N_4 [31,44], while the single shoulder at ca. 532 nm is due to the oxygen vacancy (Vo) as well as the hybridization of 4s and 4p orbital states in the Zn and Ge belonging to Zn_2GeO_4 [43,45–47]. No major change occurred in the PL emission profile, except in terms of its intensity. This likely is due to a band alignment of type-I (straddling gap), which will be discussed in more detail below.

To confirm these findings, we carried out the Rietveld refinement analysis of the as-prepared samples. The structural parameters obtained from the Rietveld refinement method [48] are shown in Figure 1e–g. An analysis of the refined structure parameters for samples with 10 wt% (with lattice parameters a = 14.246 Å; c = 9.538 Å, and V = 1676.511 $Å^3$), 20 wt% (with lattice parameters a = 14.256 Å; c = 9.547 Å, and V = 1680.285 $Å^3$), and 40 wt% (with lattice parameters a = 14.261 Å; c = 9.551 Å, and V = 1682.254 $Å^3$) of Zn_2GeO_4, respectively, shows that they all obey to the rhombohedral structure of Zn_2GeO_4 (belonging to space group R3). Moreover, theoretical calculations show that the structural parameters of the Zn_2GeO_4/g-C_3N_4 nanocomposite, where the (001) surface was assumed as the structure that is supported (deposited above the monolayer) by the (3 × 3) g-C_3N_4 supercell, composing 105 atoms, which indicates after the optimization a lattice parameter a = b = 13.762 Å, which is only 3.4% smaller than the experimentally observed (see Figure 2a). Furthermore, a decrease was observed in the effective theoretical band gap (Egap = 3.6eV) for this nanocomposite, if compared to the bulk Zn_2GeO_4 (Egap = 4.58 eV), but it is close to the calculated value for the bulk g-C_3N_4 (Egap = 3.3 eV), indicating the obtained of a band alignment of type-I.

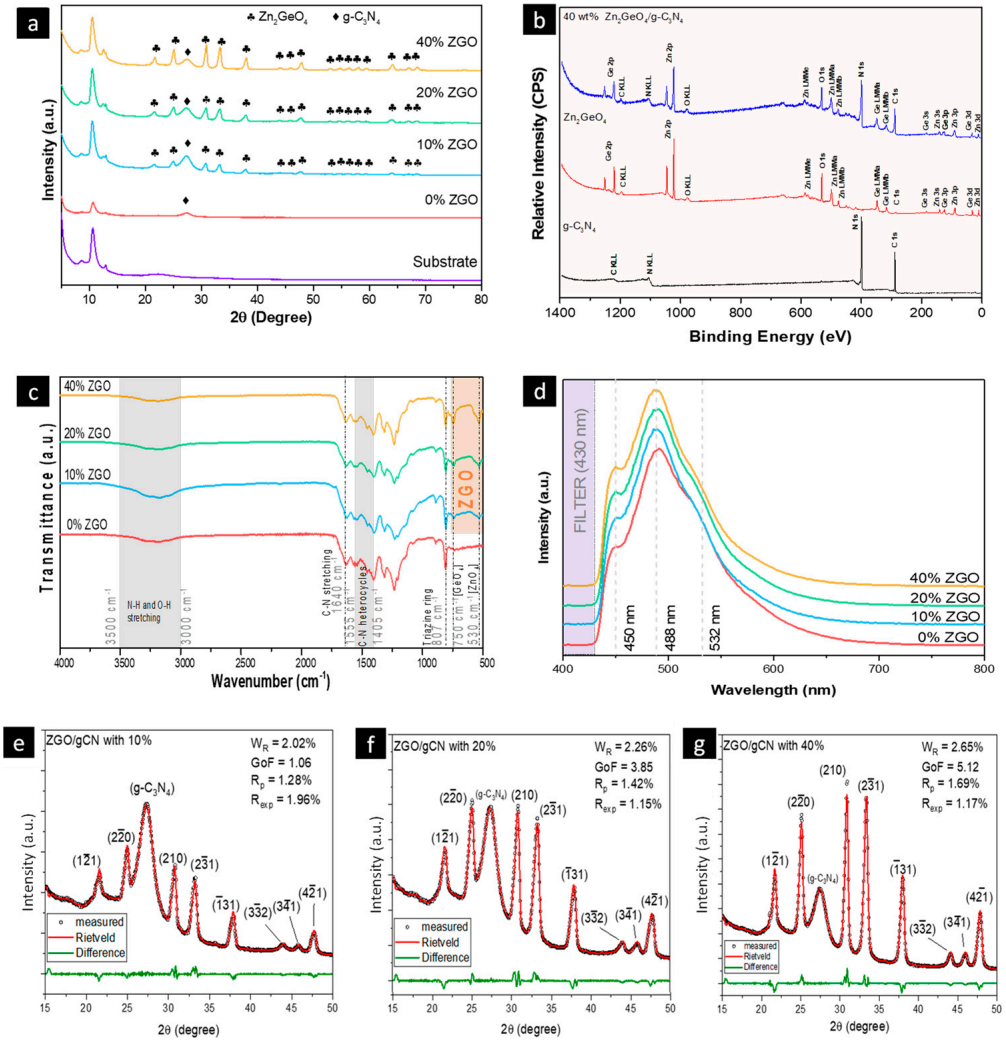

Figure 1. Structural, vibrational, and optical characterization of Zn_2GeO_4/g-C_3N_4 nanocomposites. (**a**) PXRD patterns, (**b**) XPS survey spectral, (**c**) FTIR spectral, and (**d**) PL spectral at room temperature of Zn_2GeO_4/g-C_3N_4 nanocomposites. (**e**–**g**) Fitting parameters of the Rietveld refinement data (W_R, GoF, R_p and R_{exp}) of samples prepared with 10, 20, and 40 wt% of Zn_2GeO_4, respectively.

Figure 2b shows the charge density distribution, which indicates that the charges over the g-C_3N_4 surface still maintain their homogeneity; however, it can be observed that there is an increase in the negative charge concentration around the Zn atoms, and a small dislocation of charge between the g-C_3N_4 and Zn_2GeO_4 layer where the layers coupling bond exists. The Mülliken charge analysis indicates that compared to the Zn_2GeO_4 bulk (~229 m|e| [Ge-O] and ~141 m|e| [Zn-O]), the overlap in the nanocomposite is slightly different (~160–288 m|e| [Ge-O] and ~105–180 m|e| [Zn-O]), and the population overlap in the C-N bonding varies from ~365 to ~460 m|e|, for both standalone and nanocomposite conformation, which is consistent with the distortion in the [ZnO_4] and [GeO_4] clusters. Moreover, we can confirm the bonding between the layers by observing that there is a non-null overlap between the Zn and N atom (~ 140 m|e|), which, along with the van der Waals interaction between the layers, makes the heterostructure more robust; and it is possible to see that there is a dislocation of the density of the Zn_2GeO_4 towards the g-C_3N_4. Consequently, these theoretical results suggest a possible strain-induced increase in the Zn-O bond length, as well as a shortening of the Ge-O bond of both tetrahedral [ZnO_4] and [GeO_4] clusters, respectively, of these nanocomposites. These results are consistent with our XRD refinement and XPS analysis and, hence, may contribute to a deep understanding of their optical and catalytic behavior.

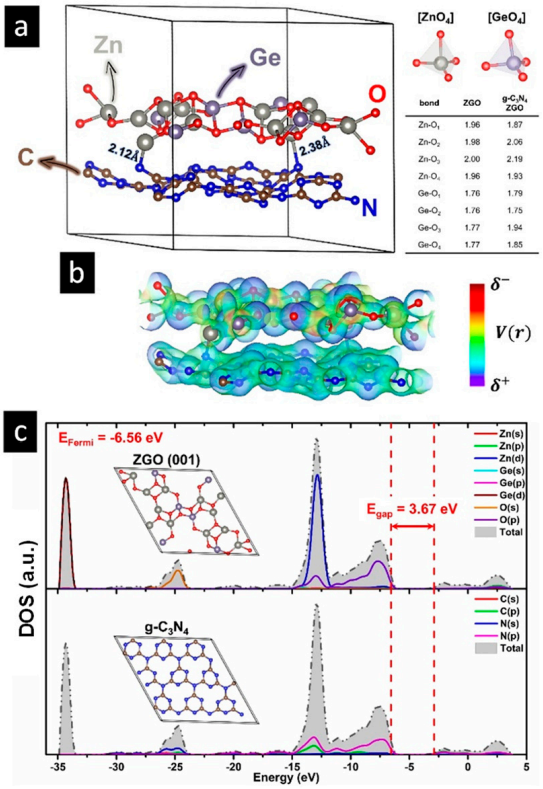

Figure 2. Theoretical assessment of the electronic structure of g-C_3N_4/Zn_2GeO_4 nanocomposite. (**a**) Representative g-C_3N_4/Zn_2GeO_4 (ZGO) nanocomposite unit cell, (**b**) Surface electrostatic potential [V(r)] for the heterostructure (0.05 a.u. isodensity), where blue and red colors denote positive and negative charge densities, respectively; (**c**) Projected density of states (PDOS) of the optimized g-C_3N_4/ZGO nanocomposite, where the upper DOS indicates the contribution of the Zn, Ge, and O orbitals, and the lower DOS the C and N atoms orbitals.

Moreover, the density of states (see Figure 2c) of the heterostructure shows that around the band gap, the O2p and N2p orbitals are the main contributions to the valence band (VB), and the O2p, Ge4p, and Zn4sp are the major contributions to the conduction band (CB). Moreover, in this case, the complete d orbitals of Zn and Ge atoms have a theoretical binding energy (BEs) for the Zn and Ge atoms in Zn_2GeO_4 bulk of about 6.49 and 25.03 eV, respectively, and for the nanocomposite it shows 6.10 and 27.58 eV, respectively, which can be compared to the experimental results found in the XPS measurements; it has a similar value for the absolute difference of the Ge, and the Zn d-center is always around ~21 eV.

Figure 3 presents selected XPS spectral windows of elemental core levels and the VB regime. The pure g-C_3N_4 sample shows the expected characteristic features, including shake-up satellites to the C 1s and N 1s lines, which indicates the high quality of this sample. The latter fine details are not easy to trace in the composite (40%) sample, because of differential charging artifacts that could not be fully removed (see experimental section). Yet, taking into account the resultant asymmetric broadening of XPS lines, an agreement is found in both the binding energies and the line intensities expected for the composite. Similarly, the Zn (see panel e in the Figure 3), Ge, and O lines of the composite are in good agreement with those of the Zn_2GeO_4 reference sample [35,46,47,49]. Moreover, these XPS results suggest a possible strain-induced increase in the length of the Zn-O bond as well as a shortening of the Ge-O bond present in both tetrahedral [ZnO_4] and [GeO_4] clusters, respectively, of these nanocomposites, which is consistent with our PXRD refinement. Table 1 presents the detailed binding energies (BE) values of the three samples. Thus, the correction terms obtained here under eFG operation are: 4.6 eV for g-C_3N_4, 4.4 eV for Zn_2GeO_4, and 4.4 eV for 40 wt% of Zn_2GeO_4/g-C_3N_4 nanocomposite, respectively.

Table 1. BE values (in eV) after correcting for charging by assuming the C 1s of adventitious carbon (indicated as CH in Figure 2a) to be at 284.8 eV (with reservation that this value is not necessarily the correct one for the present systems).

	$g\text{-}C_3N_4$	Zn_2GeO_4	40% Zn_2GeO_4
C (main)	283.3	-	288.35
N (main)	398.6	-	398.92
Zn 2p 3/2	-	1022.15	10.22
Zn 3d	-	10.83	10.95
Ge 3d	-	32.25	32.5
O	-	531.25	531.3
XPS VB (top)	2.53	3.83 (3.15)	2.9–3.03

A notable result regards the XPS VB spectrum. The top of the VB of pure $g\text{-}C_3N_4$ appears at binding energy significantly lower than that of the pure Zn_2GeO_4. Therefore, a physical mixture of two non-interacting constituents would be expected to integrally have its top of VB at a value that aligns with that of the pure $g\text{-}C_3N_4$. As shown in Figure 3f, the experimental result is very different: As such, the composite top of VB is at binding energy significantly higher, about 0.5 eV, than that of pure $g\text{-}C_3N_4$. This result indicates the emergence of charge transfer between the two constituents. Further details on the charge transfer are probably hidden in the line shapes of the elemental lines, to which our access is limited due to the inhomogeneous charging discussed above. Yet, the evidence provided by the XPS VB spectra is easily resolved and, thus, provides an efficient indicator of the interaction between the composite constituents [14,35–37]. Besides, the analysis of the VB position in the XPS spectrum of the Zn_2GeO_4 and $g\text{-}C_3N_4$ samples and theoretical calculations confirm, thereby, a type-I band alignment for these nanocomposites is obtained.

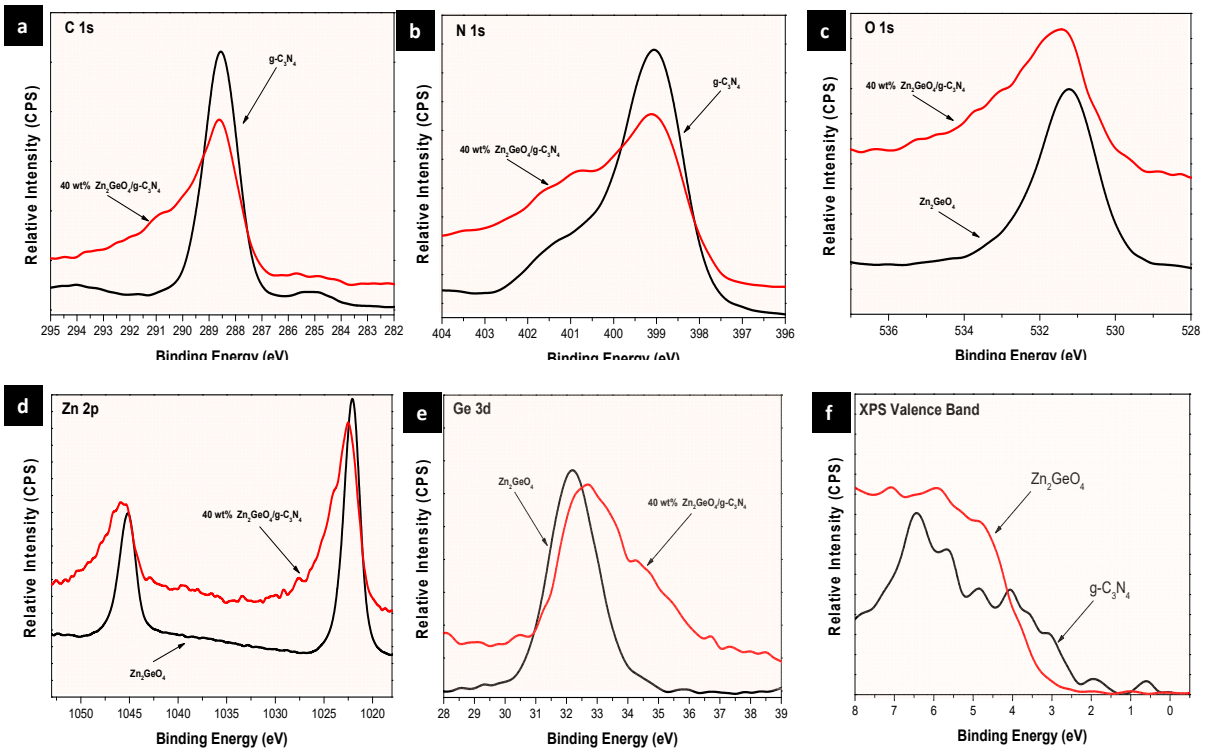

Figure 3. Representative XPS spectral windows of the reference materials and the 40 wt% of $Zn_2GeO_4/g\text{-}C_3N_4$ nanocomposite, showing the (**a**) C 1s, (**b**) N 1s, (**c**) O 1s, (**d**) Zn 2p, and (**e**) Ge 3d lines. The valence bands window of both $g\text{-}C_3N_4$ and Zn_2GeO_4 samples (**f**), as indicated. Note that the composite lines are subject to differential charging, due to which asymmetric broadening tails are encountered.

We also find that these nanocomposites show high chemical reactivity in photocatalysis. Figure 4a–d shows the results of a photocatalysis test: the degradation of MB solution by well-defined Zn_2GeO_4/g-C_3N_4 nanocomposites (designated as Zn_2GeO_4 together with the wt% of Zn_2GeO_4). Table 2 lists the corresponding catalytic degradation reaction rate constant. The kinetic constant (k) shows a considerable variation, from 6.5×10^{-3} min^{-1} for ZGO (40 wt%) to 3.4×10^{-3} min^{-1} for ZGO (0%), suggesting that the presence of Zn_2GeO_4 nanocrystals significantly accelerates the photocatalytic degradation of MB in solution. In addition, the correlation coefficient (R^2) values are consistent with the following pseudo-first-order kinetic model [47].

Table 2. Photocatalysis parameters of Zn_2GeO_4/g-C_3N_4 nanocomposite.

Sample	k [10^{-3} min^{-1}]	R^2 [%]	Adsorption [%]	Degradation [%]
0% ZGO	3.44	96.77	35.53	46.73
10% ZGO	2.64	99.57	7.42	38.26
20% ZGO	4.25	98.28	6.51	56.12
40% ZGO	6.54	99.35	6.05	70.52

Generally, with the adjustment of process parameters, the resulting materials can be modified to contain varying numbers of defect states in the interior of the bandgap [49–53]. From an electronic perspective, the disorder is characterized by energy states above the VB and below the CB; it decreases the bandgap by the optically measured gap [20]. It is reported that H_2O and O_2 molecules are dissociated in the resulting oxygen vacancy, producing the active species $^{\bullet}OH$ and $^{\bullet}O^{2-}$ [47]. Hence, such complex defects a priori can act as sites more effective for promoting adsorption, leading to improved photocatalytic response [47,49–53]. Therefore, the high photocatalytic activity of the compounds with 20 wt% and 40 wt% Zn_2GeO_4, compared to those with 0 wt% and 10 wt% Zn_2GeO_4, can be related to the high density of the oxygen vacancies, and a synergistic effect between the Zn_2GeO_4 and g-C_3N_4. It also reflects an effective charge separation efficiency and high capacity for utilizing visible light by these nanocomposites [14].

Additionally, the degradation rate obtained in this study was also compared to other heterostructure-based photocatalysts reported in the literature. These results are summarized in Table 3. We can observe that the Zn_2GeO_4/g-C_3N_4 nanocomposites have a satisfactory photocatalytic activity and, hence, can be considered promising for the treatment of effluents with complex characteristics.

Table 3. Comparison with other photocatalysts for the degradation of MB solution.

Material	k (10^{-3} min^{-1})	Ref.
This work	6.54	-
NiO/Cd/g-C_3N_4	2.4	[54]
Fe_2O_3/g-C_3N_4	9.2	[55]
ZnO/g–C_3N_4	14	[56]
Mo-doped $NiTiO_3$/g-C_3N_4	0.88	[57]

Figure 5a shows SEM images of the sample with 40 wt% of Zn_2GeO_4, and a proposed photocatalytic degradation mechanism. The SEM images demonstrate the formation of interfacial contact between g-C_3N_4 and Zn_2GeO_4 components. Because g-C_3N_4 has a higher work function than Zn_2GeO_4, of course, electrons move from the Zn_2GeO_4 structure to the g-C_3N_4 structure until they reach Fermi level equilibrium, thereby generating an internal electric field at the interface of the two phases [11,13,14,31,45]. Thus, with visible light excitation, g-C_3N_4 is much easier to excite and generate charge carriers as well. Our results revealed a band alignment of type-I for Zn_2GeO_4/g-C_3N_4 interface (Figure 4f), in agreement with the literature [14,31,45]. As a consequence, $^{\bullet}O^{2-}$ and $^{\bullet}OH$ are the active

species for the MB photocatalysis process, which is consistent with the experimental results shown in Figure 5. This synergistic effect resulting from type-I band alignment between g-C_3N_4 and Zn_2GeO_4 compounds can, in principle, accelerate the effective separation of the photoexcited charges at the interface, both, thus, improving the optical and catalytic performance of well-defined Zn_2GeO_4/g-C_3N_4 nanocomposites [11,13,14,31,45].

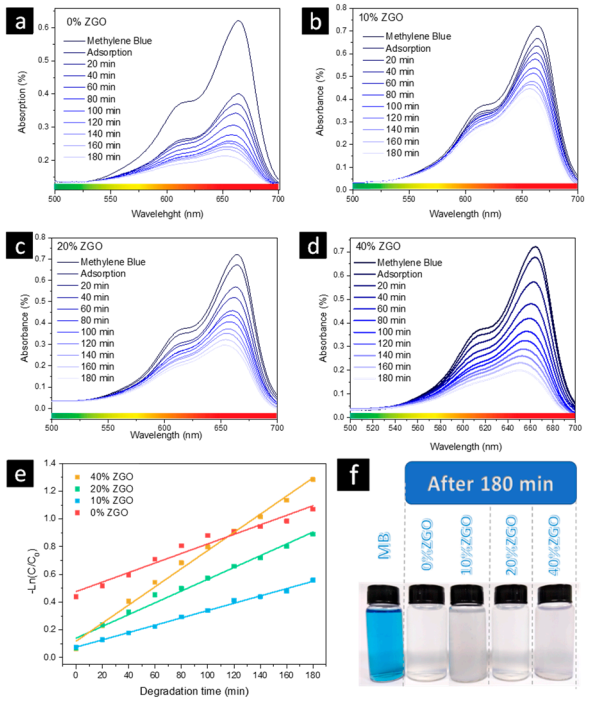

Figure 4. Photocatalytic activity of Zn_2GeO_4/g-C_3N_4 nanocomposites. (**a**–**d**) Results of UV-vis absorption spectra of MB solutions containing Zn_2GeO_4/g-C_3N_4 nanocomposites at various irradiation times, (**e**) first-order kinetics plots, and (**f**) digital photos of MB solutions after photocatalysis reaction.

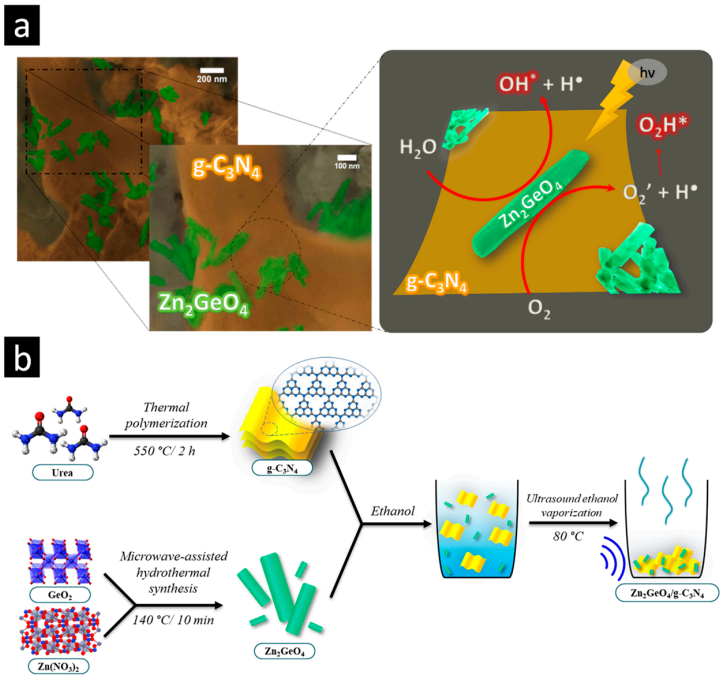

Figure 5. (**a**) SEM images and the tentative photocatalytic degradation mechanism over Zn_2GeO_4/g-C_3N_4 nanocomposites. (**b**) Scheme of Zn_2GeO_4, g-C_3N_4 and Zn_2GeO_4/g-C_3N_4 composite synthesis.

3. Materials and Methods

3.1. Synthesis of Zn_2GeO_4 Nanorods

The Zn_2GeO_4 nanorods were synthesized by the microwave-assisted hydrothermal at 140 °C for 10 min according to the method as described in our previous works [46,47].

3.2. Synthesis of g-C_3N_4

The g-C_3N_4 sample was carried out by the thermal polymerization of urea according to the method as described in our previous work [31].

3.3. Preparation of Zn_2GeO_4/g-C_3N_4 Nanocomposite

Here, the Zn_2GeO_4/g-C_3N_4 nanocomposite was prepared by the ultrasound-assisted solvent method. It was used 10, 20, and 40 wt% of Zn_2GeO_4 relative to the amount of g-C_3N_4 (ca. 0.3 g). Then, the g-C_3N_4 and Zn_2GeO_4 was mixed in 30.0 mL of ethanol and placed in an ultrasonic bath (Ya-Xun 3060, 42 kHz, 50 W) at 80 °C, until all the ethanol evaporates. A summary of the whole process of preparation can be observed by the process outlined in Figure 5b.

3.4. Materials Characterization

The powder X-ray diffraction (PXRD) patterns of as-prepared samples were obtained using Bruker/D2Phaser with Cu Kα radiation (λ = 1.5406 Å). The 2θ range was 5–80°, and the scanning rate was 0.01°s^{-1}. Next, the obtained PXRD patterns of as-prepared samples were also analyzed by the Rietveld refinement method [48] using the GSAS II [58]. FTIR spectroscopy was carried out in the 500–4000 cm^{-1} range using a PerkinElmer spectrophotometer in the attenuated total reflectance mode. Morphologies of the samples were then observed from a field emission gun scanning electron microscopy (JEOL 7001F, Tokyo, Japan).

Excitation pulses were generated by a frequency tripled Nd:YAG Q-switched laser oscillator pumping an optical parametric oscillator (OPO) (model: NT342/C/3/UVE, EKSPLA) with pulse durations of ~5 ns at a repetition rate of 10 Hz. Excitation pulses at 420 nm were obtained from the OPO. The emitted signals from the samples were spectrally filtered and passed through a 435 long-pass filter and focused into a 10 × 10 mm rectangular quartz cuvette (Starna Cells), containing a solution of a low concentration of the samples dispersed in isopropanol, and stirred continuously with a magnetic stirrer. Here, Zn_2GeO_4, g-C_3N_4 were used as the reference samples and varied concentrations of (10, 20, and 40 wt% of Zn_2GeO_4)-g-C_3N_4 were compared with them. XPS measurements were performed on a Kratos AXIS-Ultra DLD spectrometer, using a monochromatic Al kα source at relatively low power, in the range of 15–75 W and detection pass energies of 20–80 eV. The base pressure in the analysis chamber was kept below $1 \cdot 10^{-9}$ torr. Due to strong effects of differential charging encountered in part of the samples, small area scans (with analysis spots 110 µm in diameter) were also included, such as to better differentiate the artifact distortions from relevant chemical information. Repeated scans on a given spot were further used for the evaluation of beam-induced effects, starting with short, low flux scans, and gradually increasing both flux and dwell time such as to gain statistics.

In addition, the Zn_2GeO_4, g-C_3N_4, and Zn_2GeO_4/g-C_3N_4 structures were also investigated based on density functional theory (DFT) calculations, as implemented in the CRYSTAL17 software [59]. All periodic DFT calculations were performed at the HSE06 functional level [60] with the Zn, Ge, and O atomic centers being described by 86-411d31G, 9-7631(511d)G, and 8-411d1 basis set, and the C and N being described using the Triple-zetta Plus Polarization (TZVP) basis set [61]. The simulations show that the optimized structural parameters of the Zn_2GeO_4 bulk are a = b = 14.317 Å (~0.6%) and c = 9.571 Å (~0.4%); and for the g-C_3N_4 bulk with a = b = 4.749 Å (~0.5%), where the percentage in the parenthesis is the deviation compared to our experimental data. In this study, the Zn_2GeO_4/g-C_3N_4 nanocomposite was modeled using the (001) and (010) surfaces of the Zn_2GeO_4, where at first a slab in the respective direction was done and then fully optimized.

After that, it was verified that the (001) surface has the same hexagonal conformation as the g-C_3N_4, making it possible to deposit this thin film of Zn_2GeO_4 on the surface of the g-C_3N_4. For that purpose, a (3 × 3) supercell of g-C_3N_4 was built and the structures were merged into one, with a distance between the layers of 4Å. In addition, the theoretical BE values were estimated in this study according to our previous works [62,63]. Here, the SCF convergence criteria were controlled by a set of five thresholds (10^{-8}, 10^{-8}, 10^{-8}, 10^{-8}, 10^{-16}), in which these parameters correspond, respectively, to the overlap and penetration for Coulomb integrals, the overlap for HF exchange integrals, and the last two thresholds for the pseudo-overlap in HF exchange series; and for both Pack–Monkhorst and Gilat shrinking factor of 8, for both bulk Zn_2GeO_4 and g-C_3N_4 [59,64]. However, in the case of the Zn_2GeO_4/g-C_3N_4 nanocomposite, due to the increase of the computational costs, since the symmetry is fully broken, using the respective values of thresholds (10^{-7}, 10^{-7}, 10^{-7}, 10^{-7}, 10^{-14}) and for both Pack–Monkhorst and Gilat shrinking factor of 2. Furthermore, the geometric tolerances adopted during the optimization procedure were set to 0.0001 and 0.0004 Ha/bohr, respectively [59]. The projected DOS was analyzed with the same k-point in the sampling employed by the optimization procedure for the diagonalization of the Fock/Kohn-Sham matrix and, thus, plotted using the XCrysden software [65].

3.5. Measurement of Photocatalytic Activity

Briefly, 50 mg of the as-prepared catalyst was dispersed in 80 mL of MB (10 mgL^{-1}) aqueous solution and was mixed at a stirring rate of 300 rpm in the dark for 20 min [53]. For carrying out the photocatalytic experiment, the mixture was placed in a self-made ultraviolet (UV) reactor with three UVC lamps 254 nm (15W, G15T8/OF, OSRAM) at the same stirring rate. An aliquot of 1 mL solution was collected every 20 min. Then, the UV-Vis absorption spectra of the collected supernatant liquid were diluted in 1 mL of water and recorded using a Libra biochrom S60 spectrophotometer in the range of 400 nm to 700 nm. All the procedures were performed at room temperature.

4. Conclusions

We have investigated the effect of Zn_2GeO_4 concentration on the structural, optical, and photocatalytic properties of Zn_2GeO_4/g-C_3N_4 nanocomposites prepared using the ultrasound-assisted solvent method. In this work, PXRD, FTIR, XPS, SEM, PL, and photocatalytic techniques, together with theoretical calculations based on periodic models, were employed to establish the structure–property relationship for Zn_2GeO_4/g-C_3N_4 nanocomposites. These results show that these nanocomposites are basically formed by the interaction of Zn_2GeO_4 nanorods (belonging to space group R3) and g-C_3N_4 nanosheets (belonging to space group P6m2). The results showed that an increased mass ratio of Zn_2GeO_4 to g-C_3N_4 can significantly improve their optical and photocatalytic responses.

By the combination of theoretical and experimental approaches, we have noted a possible strain-induced increase in the Zn-O bond length, as well as a shortening of the Ge-O bond of both tetrahedral [ZnO_4] and [GeO_4] clusters, respectively, in Zn_2GeO_4 lattice of these nanocomposites. These results suggest that the disordered structure promotes local polarization and a charge gradient in the interfacial contact, which has a band alignment of type-I (as confirmed by analysis of the XPS VB spectrum and DFT calculations), i.e., resulting in significantly improving the optical and visible-light-induced photodegradation performance of well-defined Zn_2GeO_4/g-C_3N_4 nanocomposites and, thus, helping in the interpretation of these results. Therefore, in this perspective, we believe that such studies may provide further chemical insight into the new advanced materials designed. In short, these nanocomposites are environmentally significant because their degradation effectiveness means that they can be widely used in the treatment of dangerous chemical residues as well as in emerging optoelectronic technologies.

Author Contributions: V.Y.S., L.H.C.A., S.D., G.S.L.F. Conceptualization, methodology, software, validation, formal analysis, investigation, data curation, writing—original draft preparation. J.R.S., H.C., D.O., F.A.L.P. Conceptualization, resources, formal analysis, investigation, data curation, writing—review and editing, supervision, project administration, funding acquisition. All authors have read and agreed to the published version of the manuscript.

Funding: This research received no external funding.

Acknowledgments: The authors gratefully acknowledge the support from the Brazillian agencies, CNPq (307213/2021-8), CAPES (grant no. 88887.467334/2019-00), FAPESP (2019/08928-9, 2022/03959-6, 2013/07296-2) and Fundação Araucária, and also Projects of International Cooperation and Exchanges NSFC (Grant no. 51561145007). The authors also thank M. A. T. da Silva for the PL measurements. The computational facilities were supported by resources supplied by the Molecular Simulations Laboratory (São Paulo State University, Bauru, Brazil).

Conflicts of Interest: The authors declare no conflict of interest.

References

1. Borges, W.M.S.; Guerreiro, M.C.; Anconi, C.P.A.; Magalhães, K.T.; Castro, G.M.M.; Neto, J.L.; Rossi, M.A.L.S. Coordination of iron (III) to modified silica surface containing pyrazine acid groups and its application in advanced oxidative processes. *Surf. Interfaces* **2022**, *29*, 10770. [CrossRef]
2. Bento, A.C.; Emídio, E.S.; Hammer, P.; Nogueira, R.F.P. Degradation of Acid Red 8 Dye Using Photo-Fenton Reaction Mediated by Titanium Modified Catalysts. *J. Braz. Chem. Soc.* **2019**, *30*, 2170–2181. [CrossRef]
3. Camargo, L.P.; Lucilha, A.C.; Gomes, G.A.B.; Liberatti, V.R.; Andrello, A.C.; da Silva, P.R.C.; Dall'Antonia, L.H. Copper pyrovanadate electrodes prepared by combustion synthesis: Evaluation of photoelectroactivity. *J. Solid State Electrochem.* **2020**, *24*, 1935–1950. [CrossRef]
4. Robinson, T.; McMullan, G.; Marchant, R.; Nigam, P. Remediation of dyes in textile effluent: A critical review on current treatment technologies with a proposed alternative. *Bioresour. Technol.* **2001**, *77*, 247–255. [CrossRef]
5. Alkanad, K.; Hezam, A.; Sujay Shekar, G.C.; Drmosh, Q.A.; Amrutha Kala, A.L.; AL-Gunaid, M.Q.A.; Lokanath, N.K. Magnetic recyclable α-Fe_2O_3–Fe_3O_4/Co_3O_4–CoO nanocomposite with a dual Z-scheme charge transfer pathway for quick photo-Fenton degradation of organic pollutants. *Catal. Sci. Technol.* **2021**, *11*, 3084–3097. [CrossRef]
6. Sharma, G.; Kumar, A.; Naushad, M.; Thakur, B.; Vo, D.V.; Gao, B.; Al-Kahtani, A.A.; Stadler, F.J. Adsorptional-photocatalytic removal of fast sulphon black dye by using chitin-cl-poly(itaconic acid-co-acrylamide)/zirconium tungstate nanocomposite hydrogel. *J. Hazard. Mater.* **2021**, *416*, 125714. [CrossRef]
7. Ivetić, T.B.; Finčur, N.L.; Šojić Merkulov, D.V.; Despotović, V.N.; Četojević-Simin, D.D.; Armaković, S.J.; Uzelac, M.M.; Bognár, S.I.; Zec, N.J.; Lukić-Petrović, S.R.; et al. Water-Active Titanium/Molybdenum/Mixed-Oxides: Removal Efficiency of Organic Water Pollutants by Adsorption and Photocatalysis and Toxicity Assessment. *Catalysts* **2021**, *11*, 1054. [CrossRef]
8. Costa, G.S.; Costa, M.J.; Oliveira, H.G.; Lima, L.C.; Luz, G.E.; Cavalcante, L.S.; Santos, R.S. Effect of the applied potential condition on the photocatalytic properties of Fe_2O_3 | WO_3 heterojunction films. *J. Inorg. Organomet. Polym.* **2020**, *30*, 2851–2862. [CrossRef]
9. Ayodhya, D.; Veerabhadram, G. A review on recent advances in photodegradation of dyes using doped and heterojunction based semiconductor metal sulfide nanostructures for environmental protection. *Mater. Today Energy* **2018**, *9*, 83–113. [CrossRef]
10. Bai, H.; Li, X.; Zhao, Y.; Fan, W.; Liu, Y.; Gao, Y.; Xu, D.; Ding, J.; Shi, W. Fabrication of $BiVO_4$-Ni/Co_3O_4 photoanode for enhanced photoelectrochemical water splitting. *Appl. Surf. Sci.* **2021**, *538*, 148150. [CrossRef]
11. Marschall, R. Semiconductor Composites: Strategies for Enhancing Charge Carrier Separation to Improve Photocatalytic Activity. *Adv. Funct. Mater.* **2014**, *24*, 2421–2440. [CrossRef]
12. Kumar, A.; Sharma, S.K.; Sharma, G.; Guo, C.; Vo, D.V.; Iqbal, J.; Naushad, M.; Stadler, F.J. Silicate glass matrix@Cu_2O/$Cu_2V_2O_7$ p-n heterojunction for enhanced visible light photo-degradation of sulfamethoxazole: High charge separation and interfacial transfer. *J. Hazard. Mater.* **2021**, *402*, 123790. [CrossRef] [PubMed]
13. Li, X.; Feng, Y.; Li, M.; Li, W.; Wei, H.; Song, D. Smart hybrids of Zn_2GeO_4 nanoparticles and ultrathin gC_3N_4 layers: Synergistic lithium storage and excellent electrochemical performance. *Adv. Funct. Mater.* **2015**, *25*, 6858–6866. [CrossRef]
14. Pei, L.; Xu, Y.; Liu, J.; Wu, J.; Han, Y.; Zhang, X. Effects of solvent-induced morphology evolution of Zn_2GeO_4 on photocatalytic activities of g-C_3N_4/Zn_2GeO_4 composites. *J. Am. Ceram. Soc.* **2019**, *102*, 6517–6528. [CrossRef]
15. Zhang, L.; Zhang, Q.; Jiu, H.; He, G. Preparation of g-C_3N_4/Zn_2GeO_4 heterojunctions with enhanced photocatalytic activity under visible light. *J. Mater. Sci. Mater. Electron.* **2016**, *27*, 7311–7317. [CrossRef]
16. Wang, S.; Li, C.; Wang, T.; Zhang, P.; Li, A.; Gong, J. Controllable synthesis of nanotube-type graphitic C_3N_4 and their visible-light photocatalytic and fluorescent properties. *J. Mater. Chem. A* **2014**, *2*, 2885–2890. [CrossRef]
17. Qian, X.; Meng, X.; Sun, J.; Jiang, L.; Wang, Y.; Zhang, J.; Hu, X.; Shalom, M.; Zhu, J. Salt-Assisted Synthesis of 3D Porous g-C_3N_4 as a Bifunctional Photo- and Electrocatalyst. *ACS Appl. Mater. Interfaces* **2019**, *11*, 27226–27232. [CrossRef]
18. Zhou, C.; Shi, R.; Shang, L.; Wu, L.Z.; Tung, C.H.; Zhang, T. Template-free large-scale synthesis of g-C_3N_4 microtubes for enhanced visible light-driven photocatalytic H_2 production. *Nano Res.* **2018**, *11*, 3462–3468. [CrossRef]

19. de Jesus, J.; Santos, A.C.; Pinto, F.M.; Taft, C.A.; La Porta, F.A. Review: Theoretical and experimental investigation of the intrinsic properties of Zn_2GeO_4 nanocrystals. *J. Mater. Sci.* **2021**, *56*, 4552–4568. [CrossRef]
20. Li, J.; Diao, X.; Xiao, Y.; Qin, L.; Lin, H.; Li, Q.; Liao, B. Effect of surfactant SDS on the morphology and photocatalytic performance of Zn_2GeO_4 nanorods. *Mater. Res. Express* **2020**, *7*, 085005. [CrossRef]
21. La Porta, F.A.; Taft, C.A. *Emerging Research in Science and Engineering Based on Advanced Experimental and Computational Strategies*; Springer: Cham, Switzerland, 2020; pp. 1–530.
22. Longo, E.; La Porta, F.A. *Recent Advances in Complex Functional Materials: From Design to Application*; Springer: Cham, Switzerland, 2017; pp. 1–454.
23. La Porta, F.A.; Taft, C.A. (Eds.) *Functional Properties of Advanced Engineering Materials and Biomolecules*, 1st ed.; Springer International Publishing: Cham, Switzerland, 2021; ISBN 978-3-030-62225-1.
24. Oliveira, L.H.; Ramírez, M.A.; Ponce, M.A.; Ramajo, L.A.; Albuquerque, A.R.; Sambrano, J.R.; Longo, E.; Castro, M.S.; La Porta, F.A. Optical and gas-sensing properties, and electronic structure of the mixed-phase $CaCu_3Ti_4O_{12}/CaTiO_3$ composites. *Mater. Res. Bull.* **2017**, *93*, 47–55. [CrossRef]
25. Diez-Cabanes, V.; Morales-Garcia, A.; Illas, F.; Pastore, M. Tuning the Interfacial Energetics in WO_3/WO_3 and WO_3/TiO_2 Heterojunctions by Nanostructure Morphological Engineering. *J. Phys. Chem. Lett.* **2021**, *12*, 11528–11533. [CrossRef] [PubMed]
26. Hossain, M.N.; Prslja, P.; Flox, C.; Muthuswamy, N.; Sainio, J.; Kannan, A.M.; Suominen, M.; Lopez, N.; Kallio, T. Temperature dependent product distribution of electrochemical CO_2 reduction on CoTPP/MWCNT composite. *Appl. Catal. B* **2022**, *304*, 120863. [CrossRef]
27. Liu, J. Origin of High Photocatalytic Efficiency in Monolayer g-C_3N_4/CdS Heterostructure: A Hybrid DFT Study. *J. Phys. Chem. C* **2015**, *119*, 28417–28423. [CrossRef]
28. Le Bahers, T.; Rérat, M.; Sautet, P. Semiconductors Used in Photovoltaic and Photocatalytic Devices: Assessing Fundamental Properties from DFT. *J. Phys. Chem. C* **2014**, *118*, 5997–6008. [CrossRef]
29. Liu, W.; Li, Y.; Liu, F.; Jiang, W.; Zhang, D.; Liang, J. Visible-light-driven photocatalytic degradation of diclofenac by carbon quantum dots modified porous g-C_3N_4: Mechanisms, degradation pathway and DFT calculation. *Water Res.* **2019**, *151*, 9–19. [CrossRef] [PubMed]
30. Chan, M.K.Y.; Ceder, G. Efficient Band Gap Prediction for Solids. *Phys. Rev. Lett.* **2010**, *105*, 196403. [CrossRef]
31. Amorin, L.H.; Suzuki, V.Y.; de Paula, N.H.; Duarte, J.L.; da Silva, M.A.T.; Taft, C.A.; La Porta, F.A. Electronic, structural, optical, and photocatalytic properties of graphitic carbon nitride. *New J. Chem.* **2019**, *43*, 13647–13653. [CrossRef]
32. Yuan, Y.; Zhang, L.; Xing, J.; Utama, M.I.; Lu, X.; Du, K.; Li, Y.; Hu, X.; Wang, S.; Genç, A.; et al. High-yield synthesis and optical properties of g-C_3N_4. *Nanoscale* **2015**, *7*, 12343–12350. [CrossRef]
33. Yuan, X.; Zhou, C.; Jin, Y.; Jing, Q.; Yang, Y.; Shen, X.; Tang, Q.; Mu, Y.; Du, A.K. Facile synthesis of 3D porous thermally exfoliated g-C3N4 nanosheet with enhanced photocatalytic degradation of organic dye. *J. Colloid Interface Sci.* **2016**, *468*, 211–219. [CrossRef]
34. Li, X.; Zhang, J.; Shen, L.; Ma, Y.; Lei, W.; Cui, Q.; Zou, G. Preparation and characterization of graphitic carbon nitride through pyrolysis of melamine. *Appl. Phys. A Mater. Sci. Process.* **2009**, *94*, 387–392. [CrossRef]
35. Su, L.; Qi, Y.; Jia, C.-J.; Jin, Z.; Fan, W. Enhanced visible-light photocatalytic activity of g-C_3N_4/Zn_2GeO_4 heterojunctions with effective interfaces based on band match. *Nanoscale* **2014**, *6*, 2649–2659.
36. Thurston, J.H.; Hunter, N.M.; Cornell, K.A. Preparation and characterization of photoactive antimicrobial graphitic carbon nitride (g-C_3N_4) films. *RSC Adv.* **2016**, *6*, 42240–42248. [CrossRef] [PubMed]
37. Wagner, C.D.; Muilenberg, G.E. *Handbook of X-ray Photoelectron Spectroscopy: A Reference Book of Standard Data for Use in X-ray Photoelectron Spectroscopy*; Physical Electronics Division, Perkin-Elmer Corp.: Eden Prairie, MN, USA, 1979.
38. Boonprakob, N.; Wetchakun, N.; Phanichphant, S.; Waxler, D.; Sherrell, P.; Nattestad, A.; Chen, J.; Inceesungvorn, B. Enhanced visible-light photocatalytic activity of g-C_3N_4/TiO_2 films. *J. Colloid Interface Sci.* **2014**, *417*, 402–409. [CrossRef]
39. Chidhambaram, N.; Ravichandran, K. Single step transformation of urea into metal-free g-C_3N_4 nanoflakes for visible light photocatalytic applications. *Mater. Lett.* **2017**, *207*, 44–48. [CrossRef]
40. Zhang, R.; Zhang, X.; Liu, S.; Tong, J.; Kong, F.; Sun, N.; Han, X.; Zhang, Y. Enhanced photocatalytic activity and optical response mechanism of porous graphitic carbon nitride (g-C_3N_4) nanosheets. *Mater. Res. Bull.* **2021**, *140*, 111263. [CrossRef]
41. Yamaguchi, O.; Hidaka, J.I.; Hirota, K. Formation and characterization of alkoxy-derived Zn_2GeO_4. *J. Mater. Sci. Lett.* **1991**, *10*, 1471–1474. [CrossRef]
42. Viegas, J.I.; Moreira, R.L.; Dias, A. Optical-vibration and intrinsic dielectric properties of low-k high-Q Zn_2GeO_4 ceramics. *J. Phys. Chem. Solids* **2021**, *148*, 109693. [CrossRef]
43. Duan, X.; Yuan, M.; Ou, K.; Zhao, W.; Tian, T.; Duan, W.; Zhang, X.; Yi, L. Controlled preparation of undoped Zn_2GeO_4 microcrystal and the luminescent properties resulted from the inner defects. *Mater. Today Commun.* **2021**, *27*, 102359. [CrossRef]
44. Alaghmandfard, A.; Ghandi, K. A Comprehensive Review of Graphitic Carbon Nitride (g-C_3N_4)–Metal Oxide-Based Nanocomposites: Potential for Photocatalysis and Sensing. *Nanomaterials* **2022**, *12*, 294. [CrossRef]
45. Xie, Z.; Lu, H.; Zhang, Y.; Sun, Q.; Zhou, P.; Ding, S.; Zhang, D.W. The electronic structures and optical properties of Zn_2GeO_4 with native defects. *J. Alloys Compd.* **2015**, *619*, 368–371. [CrossRef]
46. Suzuki, V.Y.; de Paula, N.H.; Gonçalves, R.; Li, M.S.; Pereira, E.C.; Longo, E.; La Porta, F.A. Exploring effects of microwave-assisted thermal annealing on optical properties of Zn_2GeO_4 nanostructured films. *Mater. Sci. Eng. B* **2019**, *246*, 7–12. [CrossRef]

47. Suzuki, V.Y.; Amorin, L.H.; Lima, N.M.; Machado, E.G.; Carvalho, P.E.; Castro, S.B.; Alves, C.S.; Carli, A.P.; Li, M.S.; Longo, E.; et al. Characterization of the structural, optical, photocatalytic and: In vitro and in vivo anti-inflammatory properties of Mn^{2+} doped Zn_2GeO_4 nanorods. *J. Mater. Chem. C* **2019**, *7*, 8216–8225. [CrossRef]
48. Rietveld, H.M. Line profiles of neutron powder-diffraction peaks for structure refinement. *Acta Crystallogr.* **1967**, *22*, 151–152. [CrossRef]
49. Sharma, A.; Varshney, M.; Chae, K.H.; Won, S.O. Mechanistic investigations on emission characteristics from g-C_3N_4, g-C_3N_4@Pt and g-C_3N_4@Ag nanostructures using X-ray absorption spectroscopy. *Curr. Appl. Phys.* **2018**, *18*, 1458–1464. [CrossRef]
50. Shi, Q.; Zhang, X.; Liu, X.; Xu, L.; Liu, B.; Zhang, J.; Xu, H.; Han, Z.; Li, G. In-situ exfoliation and assembly of 2D/2D g-C_3N_4/TiO_2(B) hierarchical microflower: Enhanced photo-oxidation of benzyl alcohol under visible light. *Carbon* **2022**, *196*, 401–409. [CrossRef]
51. Waheed, A.; Shi, Q.; Maeda, N.; Meier, D.M.; Qin, Z.; Li, G.; Baiker, A. Strong Activity Enhancement of the Photocatalytic Degradation of an Azo Dye on Au/TiO_2 Doped with FeOx. *Catalysts* **2020**, *10*, 933. [CrossRef]
52. Sharma, G.; Kumar, A.; Sharma, S.; Naushad, M.; Dhiman, P.; Vo, D.V.; Stadler, F.J. Fe_3O_4/ZnO/Si_3N_4 nanocomposite based photocatalyst for the degradation of dyes from aqueous solution. *Mater. Lett.* **2020**, *278*, 128359. [CrossRef]
53. Suzuki, V.Y.; Amorin, L.H.; de Paula, N.H.; Albuquerque, A.R.; Li, M.S.; Sambrano, J.R.; Longo, E.; La Porta, F.A. New insights into the nature of the bandgap of $CuGeO_3$ nanofibers: Synthesis, electronic structure, and optical and photocatalytic properties. *Mater. Today Commun.* **2021**, *26*, 101701. [CrossRef]
54. Karimi, M.A.; Atashkadi, M.; Ranjbar, M.; Habibi-Yangjeh, A. Novel visible-light-driven photocatalyst of NiO/Cd/g-C_3N_4 for enhanced degradation of methylene blue. *Arab. J. Chem.* **2020**, *13*, 5810–5820. [CrossRef]
55. Karimi, M.A.; Iliyat, M.; Atashkadi, M.; Ranjbar, M.; Habibi-Yangjeh, A. Microwave-assisted synthesis of the Fe_2O_3/g-C_3N_4 nanocomposites with enhanced photocatalytic activity for degradation of methylene blue. *J. Chin. Chem. Soc.* **2020**, *67*, 2032–2041. [CrossRef]
56. Hakimi-Tehrani, M.J.; Hassanzadeh-Tabrizi, S.A.; Koupaei, N.; Saffar-Teluri, A.; Rafiei, M. Facile thermal synthesis of g–C_3N_4/ZnO nanocomposite with antibacterial properties for photodegradation of Methylene blue. *Mater. Res. Express* **2021**, *8*, 125002. [CrossRef]
57. Pham, T.-T.; Shim, E.W. Inhibition of charge recombination of $NiTiO_3$ photocatalyst by the combination of Mo-doped impurity state and Z-scheme charge transfer. *Appl. Surf. Sci.* **2020**, *501*, 143992. [CrossRef]
58. Toby, B.H.; Von Dreele, R.B. GSAS-II: The genesis of a modern open-source all purpose crystallography software package. *J. Appl. Crystallogr.* **2013**, *46*, 544–549. [CrossRef]
59. Dovesi, R.; Saunders, V.R.; Roetti, C.; Orlando, R.; Zicovich-Wilson, C.M.; Pascale, F.; Civalleri, B.; Doll, K.; Harrison, N.M.; Bush, I.J.; et al. *CRYSTAL17—User's Manual*; University of Torino: Torino, Italy, 2018.
60. Heyd, J.; Scuseria, G.E.; Ernzerhof, M. Hybrid functionals based on a screened Coulomb potential. *J. Chem. Phys.* **2003**, *118*, 8207. [CrossRef]
61. CRYSTAL—Basis Sets Library, (n.d.). Available online: http://www.crystal.unito.it/basis-sets.php (accessed on 5 April 2022).
62. La Porta, F.A.; Gracia, L.; Andrés, J.; Sambrano, J.R.; Varela, J.A.; Longo, E. A DFT Study of Structural and Electronic Properties of ZnS Polymorphs and its Pressure-Induced Phase Transitions. *J. Am. Ceram. Soc.* **2014**, *97*, 4011–4018. [CrossRef]
63. de Jesus, J.P.A.; Jimenez, M.Z.; La Porta, F.A. Theoretical investigation on the effects of electric field on the electronic structure and spectroscopic properties of $Zn_6-xCdxS_6$ clusters as model systems of semiconductor quantum dots. *Comput. Mater. Sci.* **2021**, *188*, 110147. [CrossRef]
64. Marana, N.L.; Albuquerque, A.R.; La Porta, F.A.; Longo, E.; Sambrano, J.R. Periodic density functional theory study of structural and electronic properties of single-walled zinc oxide and carbon nanotubes. *J. Solid State Chem.* **2016**, *237*, 36–47. [CrossRef]
65. Kokalj, A. XCrySDen—A new program for displaying crystalline structures and electron densities. *J. Mol. Graph. Model.* **1999**, *17*, 176–179. [CrossRef]